

# Northumbria Research Link

Citation: Mu, Hailiang, Zhuge, Xiangqun, Ren, Guogang, Luo, Kun, Ding, Zhengping, Ren, Yurong, Luo, Zhihong, Bayati, Maryam, Xu, Bin and Liu, Xiaoteng (2023) Dual Functional Mesoporous Silica Colloidal Electrolyte for Lithium-Oxygen Batteries. Chemical Engineering Journal, 455 (Part 2). p. 140761. ISSN 1385-8947

Published by: Elsevier

URL: <https://doi.org/10.1016/j.cej.2022.140761>  
<<https://doi.org/10.1016/j.cej.2022.140761>>

This version was downloaded from Northumbria Research Link:  
<https://nrl.northumbria.ac.uk/id/eprint/50784/>

Northumbria University has developed Northumbria Research Link (NRL) to enable users to access the University's research output. Copyright © and moral rights for items on NRL are retained by the individual author(s) and/or other copyright owners. Single copies of full items can be reproduced, displayed or performed, and given to third parties in any format or medium for personal research or study, educational, or not-for-profit purposes without prior permission or charge, provided the authors, title and full bibliographic details are given, as well as a hyperlink and/or URL to the original metadata page. The content must not be changed in any way. Full items must not be sold commercially in any format or medium without formal permission of the copyright holder. The full policy is available online: <http://nrl.northumbria.ac.uk/policies.html>

This document may differ from the final, published version of the research and has been made available online in accordance with publisher policies. To read and/or cite from the published version of the research, please visit the publisher's website (a subscription may be required.)

# Dual Functional Mesoporous Silica Colloidal Electrolyte for Lithium-Oxygen Batteries

Hailiang Mu<sup>1</sup>, Xiangqun Zhuge<sup>1</sup>, Guogang Ren<sup>2</sup>, Kun Luo<sup>1\*</sup>, Zhengping Ding<sup>1</sup>, Yurong Ren<sup>1</sup>,  
Zhihong Luo<sup>3\*</sup>, Maryam Bayati<sup>4</sup>, Ben Bin Xu<sup>4</sup>, Xiaoteng Liu<sup>4\*</sup>

1. Changzhou Key Laboratory of Intelligent Manufacturing and Advanced Technology for Power Battery, School of Materials Science & Engineering, Changzhou University, Changzhou 213164, P R China;

2. Department of Engineering and Technology, School of Physics, Engineering and Computer Science, University of Hertfordshire, Hatfield, Hertfordshire, AL10 9AB, UK;

3. Guangxi Key Laboratory of Optical and Electronic Materials and Devices, Guilin University of Technology, Guilin 541004, P R China;

4. Department of Mechanical and Construction Engineering, Faculty of Engineering and Environment, Northumbria University, Newcastle upon Tyne, NE1 8ST, UK.

## Abstract

Dual functional mesoporous silica (mSiO<sub>2</sub>) colloidal electrolytes are promising to protect lithium anode and accelerate the reaction kinetics on cathode for lithium-oxygen batteries (LOBs). In this work, we achieved a significantly extended battery life (from 55 to 328 cycles) of LOB by using mSiO<sub>2</sub> with a concentration of 80 mg L<sup>-1</sup> in the colloidal electrolyte, compared with the one using conventional LiClO<sub>4</sub>/DMSO electrolyte. The rate performance and full-discharge capacity are also dramatically enhanced. The as-synthesized mSiO<sub>2</sub> has a special ordered hexagonal mesoporous structure, with a high specific surface area of 1016.30 m<sup>2</sup> g<sup>-1</sup>, which can form a stable colloid after mixing with 1.0 M LiClO<sub>4</sub>/DMSO. The side reactions of Li stripping/plating are suppressed, thus the cycling life performance of LOB is enhanced by relieving the attack of superoxide intermediates. The co-deposition of mesoporous mSiO<sub>2</sub> and Li<sub>2</sub>O<sub>2</sub> also effectively accelerated the decomposition of the discharge product by promoting the mass transfer at the cathode. This investigation of suppressing side reactions using non-aqueous electrolytes will shed a new light on the design and development of novel lithium metal batteries.

**Keywords:** lithium-oxygen battery; colloidal electrolyte; mesoporous silica; cycle life

31

32 **Corresponding authors:** Prof. Kun Luo, email: [luokun@cczu.edu.cn](mailto:luokun@cczu.edu.cn); Dr. Terence Xiaoteng Liu,

33 email: [terence.liu@northumbria.ac.uk](mailto:terence.liu@northumbria.ac.uk) ; Dr. Zhihong Luo, email: [luozhihong@glut.edu.cn](mailto:luozhihong@glut.edu.cn).

34

## 35 1. Introduction

36 The lithium-oxygen battery (LOB) has been well-known for its prestige theoretical energy  
37 density ( $\approx 3500 \text{ Wh kg}^{-1}$ ) among all the state-of-the-art rechargeable batteries [1-3]. However,  
38 challenges remain in various aspects, such as sluggish decomposition of lithium peroxide ( $\text{Li}_2\text{O}_2$ ),  
39 quick depletion of lithium (Li) metal, electrolyte cleavage and intrinsic safety issues [4-6]. Dendritic  
40 growth [7,8] and corrosion of Li are common phenomena detrimental to the anode. Recent reports  
41 have shown some effective approaches to protect Li-ion anode by using solid electrolytes [9-11] or  
42 electrolyte additives [14,15]; Chemical/electrochemical pre-treatments [16,17] and the addition of  
43 artificial SEI layers [12,13] also improves the stability of Li anodes. For the cathode, oxygen reduction  
44 reaction (ORR) occurs during battery discharging. The oxygen is reduced to generate  $\text{Li}_2\text{O}_2$  crystals  
45 through diffusing into the electrolytes with high donor numbers including dimethyl sulfoxide  
46 (DMSO) and 1-methylimidazole (Me-Im) etc., and deposit on the cathode (solution pathway). There  
47 is also a surface pathway to directly react at the cathode to produce film-like  $\text{Li}_2\text{O}_2$  in the electrolytes  
48 with low donor numbers, such as dimethyl ether (DME), tetraethylene glycol dimethyl ether  
49 (TEGDME) and acetonitrile [18]. The diffusion of ORR intermediates can also trigger the  
50 decomposition of electrolytes and the corrosion of Li anodes. The discharge product during battery  
51 charging cannot go through a complete decomposition, thus tend to accumulate if the charging  
52 potential increases and lead to failure of the LOBs because of cathode passivation [19,20], due to the  
53 low solubility of  $\text{Li}_2\text{O}_2$  and the sluggish kinetics of oxygen evolution reaction (OER), the presence  
54 of byproducts and the poor mass transfer.

55 Couple of strategies have been developed to prompt the cathode reactions by preventing the  
56 deposition of the insoluble discharge product. In terms of bulk electrode modification, Peng et al.  
57 reported a porous gold (Au) cathode that maximized the content of reversible product  $\text{Li}_2\text{O}_2$  in ORR  
58 process, where 95% of the initial capacity was retained after 100 cycles [21]. Ganapathy et al.  
59 introduced NiO nanoparticles to refine  $\text{Li}_2\text{O}_2$  grains and accelerated grain decomposition to prevent  
60 cathodic passivation [22]. Hwang et al. embedded discharge product into the carbon macroscopic  
61 pores with mesoscale channels and openings connecting and found that the specific size of the pores  
62 enhanced the capacity and cyclability of the LOBs, meanwhile it inhibited the side reactions [23].  
63 The addition of catalyst, such as noble metals (Pt, Ru), transition metal oxide ( $\text{Co}_3\text{O}_4$ ,  $\text{MoO}_2$ ) and  
64 transition metal-nitrogen-carbon (Fe, Co-N-C) [24-28], also improves the performance of lithium

65 oxide battery. However, insoluble discharge product deposits on the catalyst surface cause its  
66 dysfunction. Nitrogen-doped graphene has been reported to have enhanced ORR catalytic activity  
67 while being used as cathode [29], and Au or Pd nanoparticles were attempted to decorate carbon  
68 nanotubes as active sites, to control the morphology and reduce the size of  $\text{Li}_2\text{O}_2$  [30]. Redox  
69 mediators, i.e. LiI, tetrathiafulvalene (TTF) and 2,2,6,6-tetramethyl-piperidinyloxy (TEMPO),  
70 were reported to assist the decomposition of discharge products and extend the cycle life of LOBs  
71 [31-33], but they were corrosive to Li anode.

72 Recently, the solid additives based colloidal electrolyte dispersion emerged as interesting  
73 solution [34,35], because they can adsorb on the surface of discharge product ( $\text{Li}_2\text{O}_2$ ), and effectively  
74 accelerate the OER kinetics with extra improvement of the electric conductivity of cathode. Additive  
75 materials include Au and Ag nanoparticles [37,38], organic molecular cage-protected Ru nanoclusters  
76 [36], and other solid additives. Kim *et al* found that the suspended  $\text{Li}_2\text{O}$  nanoparticles change the  $\text{Li}^+$   
77 solvation environment in aprotic electrolytes [39], and created the inorganic-rich solid-electrolyte  
78 interphases on Li anode, led to the uniform plating/stripping of Li. Mesoporous materials have been  
79 widely applied in energy storage and conversion owing to their extraordinarily high surface areas  
80 and large pore volumes [40]. Yu *et al* dispersed molecular sieve powders into the TEGDME electrolyte,  
81 where the inorganic additive adsorb superoxide ( $\text{LiO}_2$ ) in the electrolyte and allow the ORR  
82 intermediate to generate  $\text{Li}_2\text{O}_2$  by disproportionation ( $\text{LiO}_{2, \text{ad}} + \text{LiO}_{2, \text{ad}} \rightarrow \text{Li}_2\text{O}_2 + \text{O}_2$ ). The  
83 discharge capacity of LOB significantly increased 63 times, because the formation of  $\text{Li}_2\text{O}_2$  was  
84 converted from surface pathway to solution pathway [41].

85 Mesoporous silica has been a viable candidate to be used in chemical adsorption, catalytic  
86 applications and environmental remedy, due to the adjustable morphology, controllable particle size  
87 and structure, large surface area, biocompatibility, low cost, simple preparation process [42,43]. In this  
88 study, we achieve the uniform suspension of  $\text{mSiO}_2$  in electrolyte and utilized it to explicitly  
89 improve the processes on both cathode and anode, therefore, lead to an enhanced performance of  
90 LOBs. The hexagonal mesoporous structure with extremely high surface area accommodates the  
91 colloid optimised stripping/plating processes, by homogenising  $\text{Li}^+$  flux at the anode and enhancing  
92 the decomposition of by-product at the cathode. This work offers a proof of concept to suppress side  
93 reactions with mesoporous colloids and enhance the performance of LOBs, which can be potentially  
94 expanded to other lithium metal batteries.

## 95 **2. Experimental**

### 96 **2.1 Materials and Chemicals**

97 Cetyltrimethylammonium bromide (CTAB,  $\geq 99\%$ ), ethanol ( $\geq 99.7\%$ ), sodium hydroxide  
98 (NaOH,  $\geq 96.0\%$ ) and tetraethyl orthosilicate (TEOS,  $\geq 28.4\%$ ) were purchased from Sinopharm  
99 Chemical Reagent Co., Ltd., China. Multiwalled carbon nanotubes (MWNTs,  $\geq 98\%$ ), dimethyl  
100 sulfoxide (DMSO, 99.9%) and propylene carbonate (PC, 99.7%) were bought from Sigma-Aldrich.  
101 Glass fiber separator ( $d = 18\text{mm}$ , GF/D, Whatman) and carbon paper (TGP-H-060, Toray) were  
102 used directly as purchased. Lithium perchlorate ( $\text{LiClO}_4$ ,  $\geq 99.99\%$ , Sigma-Aldrich) was dried in a  
103 vacuum oven at  $120\text{ }^\circ\text{C}$  for 12 h before adding into  $1.0\text{ mol L}^{-1}\text{ LiClO}_4/\text{DMSO}$  electrolytes.  
104 Molecular sieves ( $4\text{\AA}$ , Sigma-Aldrich) after activation were added to the electrolytes for the purpose  
105 of removing any moisture for one week prior to use. Lithium sheets ( $d = 14\text{ mm}$ , Tianjin Zhongneng  
106 Lithium Industry Co., Ltd.) are immersed in  $0.1\text{ mol L}^{-1}\text{ LiClO}_4/\text{PC}$  solution for at least 3 days.

### 107 **2.2 Preparation of mesoporous silica ( $\text{mSiO}_2$ ) colloidal electrolyte**

108  $0.201\text{ g}$  of CTAB,  $10.17\text{ g}$  of ethanol,  $128\text{ g}$  of deionized water and  $0.1\text{ g}$  of NaOH were added  
109 into a round-bottomed flask, and the mixture was magnetically stirred at a rate of  $600\text{ rpm}$  and  
110 heated in an oil bath at  $30\text{ }^\circ\text{C}$  for  $30\text{ min}$ . Then,  $1\text{ g}$  of TEOS was added to the mixture and kept  
111 reacting for  $5\text{ h}$ . After standing for  $24\text{ h}$ , the mixture was centrifugally separated, and the precipitate  
112 was collected and dried in an oven at  $80\text{ }^\circ\text{C}$ . After calcinating in a muffle furnace at  $550\text{ }^\circ\text{C}$ , the  
113 resultant  $\text{mSiO}_2$  powder is obtained.

114 Different amounts of  $\text{mSiO}_2$  powders were dispersed in  $1.0\text{ mol L}^{-1}\text{ LiClO}_4/\text{DMSO}$  electrolytes  
115 colloidal electrolytes with the  $\text{mSiO}_2$  (denoted as  $\text{mSiO}_2/\text{LiClO}_4/\text{DMSO}$ ) concentrations of  $10\text{ mg}$   
116  $\text{mL}^{-1}$ ,  $30\text{ mg mL}^{-1}$ ,  $50\text{ mg mL}^{-1}$ ,  $70\text{ mg mL}^{-1}$ ,  $80\text{ mg mL}^{-1}$  and  $100\text{ mg mL}^{-1}$ , respectively.

### 117 **2.3 Battery assembly and testing**

118  $10\text{ mg}$  of MWNTs were dispersed in  $20\text{ mL}$  of ethanol under ultrasonication, the ink was  
119 sprayed uniformly on carbon paper with a loading of  $0.1\text{ mg cm}^{-2}$ . After drying for  $12\text{ h}$  in a vacuum  
120 oven at  $80\text{ }^\circ\text{C}$ , the carbon paper with MWNTs was cut into square ( $\sim 1\text{ cm}^2$ ) to be used as cathodes.  
121 Then, the coin cell (CR2032 with holes) was assembled following the sequence of “Li anode - glass  
122 fiber separator - injection of electrolyte - MWNTs cathode” in an argon-filled glove box (Nanjing  
123 Jiumen Automation Technology Co., Ltd.,  $\text{H}_2\text{O} < 0.1\text{ ppm}$ ,  $\text{O}_2 < 0.1\text{ ppm}$ ). Battery testing was  
124 performed in an oxygen atmosphere ( $\geq 99.9\%$ ). The long-term cycling was carried under a current

125 density of  $1 \text{ A g}^{-1}$  with a fixed capacity of  $1000 \text{ mAh g}^{-1}$  based on the loading amount of MWNTs,  
126 and the cut-off voltages were set up at 2.0 V and 4.5 V. The rate performance was tested with the  
127 fixed capacity of  $1000 \text{ mAh g}^{-1}$ , and current density values of  $3 \text{ A g}^{-1}$  and  $5 \text{ A g}^{-1}$  were applied. For  
128 the full-discharge test, the discharge current was set up at 0.1 mA and the cut-off voltage was 2.0 V.

129 Two types of symmetrical batteries were tested, stainless steel (SS|SS) and lithium plates (Li|Li)  
130 batteries. Glass fibre separators soaked with selected electrolytes and CR2032 coin cells (no holes)  
131 were used to test symmetrical batteries. The SS|SS symmetrical cell was employed to study the  
132 effect of suspending  $\text{mSiO}_2$  on the ionic conductivity of electrolyte, while the Li|Li cell was used to  
133 investigate the influence of colloidal electrolyte with  $\text{mSiO}_2$  on the stripping/plating of Li.

#### 134 2.4 Characterizations

135 Field emission desktop scanning electron microscope (Phenom LE, Thermo Fisher Scientific),  
136 high-resolution transmission electron microscope (JEM-2100, JEOL) and X-ray diffractometer  
137 (XRD, D/max 2500PC, Rigaku) are utilised for morphology and structure characterisation. Raman  
138 spectrometer (532 nm, DXR2, Thermo Scientific) is used for the discharge product analysis. The  
139 adsorption-desorption isotherm was tested by a Surface Area & Porosimetry System (ASAP2460,  
140 Micromeritics). Electrochemical impedance spectroscopy (EIS) testing was carried out in the  
141 frequency range from 1 MHz to 0.1 Hz by using an Electrochemical Workstation (CHI 760E,  
142 Shanghai Chenhua Instrument Co.) with an AC amplitude of 5 mV. The ionic conductivity of  
143 electrolyte was measured in a symmetrical coin cell with two stainless steel electrodes (SS|SS) by  
144 using the following equation:  $\sigma = d/R_b S$ , where  $R_b$  is the solution resistance,  $d$  represents the  
145 thickness of the glass fiber separator ( $\sim 890 \mu\text{m}$ ), and  $S$  represents the geometric area of SS electrodes.  
146 A rotating ring-disk electrode (RRDE-3A, ALS Co., Ltd.) equipped with a glassy carbon (GC, with  
147 an area of  $0.126 \text{ cm}^2$ ) disk and a Pt ring (with an area of  $0.189 \text{ cm}^2$ ) was employed to analyze the  
148 ORR catalytic activity. The GC disk electrode was modified by a pre-mixed slurry containing 4 mg  
149 of MWNTs, 100  $\mu\text{L}$  of Nafion perfluorinated resin solution, 800  $\mu\text{L}$  of  $\text{H}_2\text{O}$  and 200  $\mu\text{L}$  of ethanol.  
150 The resulting GC disk electrode was covered by a layer of MWNTs at a mass loading of  $0.1 \text{ mg cm}^{-2}$ .  
151 Pt wire was used as the counter electrode, and Ag/AgNO<sub>3</sub> was used as reference electrode (the  
152 silver wire is immersed in DMSO containing 0.1M AgNO<sub>3</sub> and calibrated in the glove box before  
153 use) [34]. The electrolyte was firstly flushed with oxygen for 30 minutes.

154

155  
156  
157  
158  
159  
160  
161  
162  
163  
164  
165  
166  
167  
168  
169  
170  
171  
172  
173  
174  
175  
176  
177  
178  
179  
180  
181  
182  
183  
184  
185  
186  
187  
188  
189  
190  
191  
192  
193

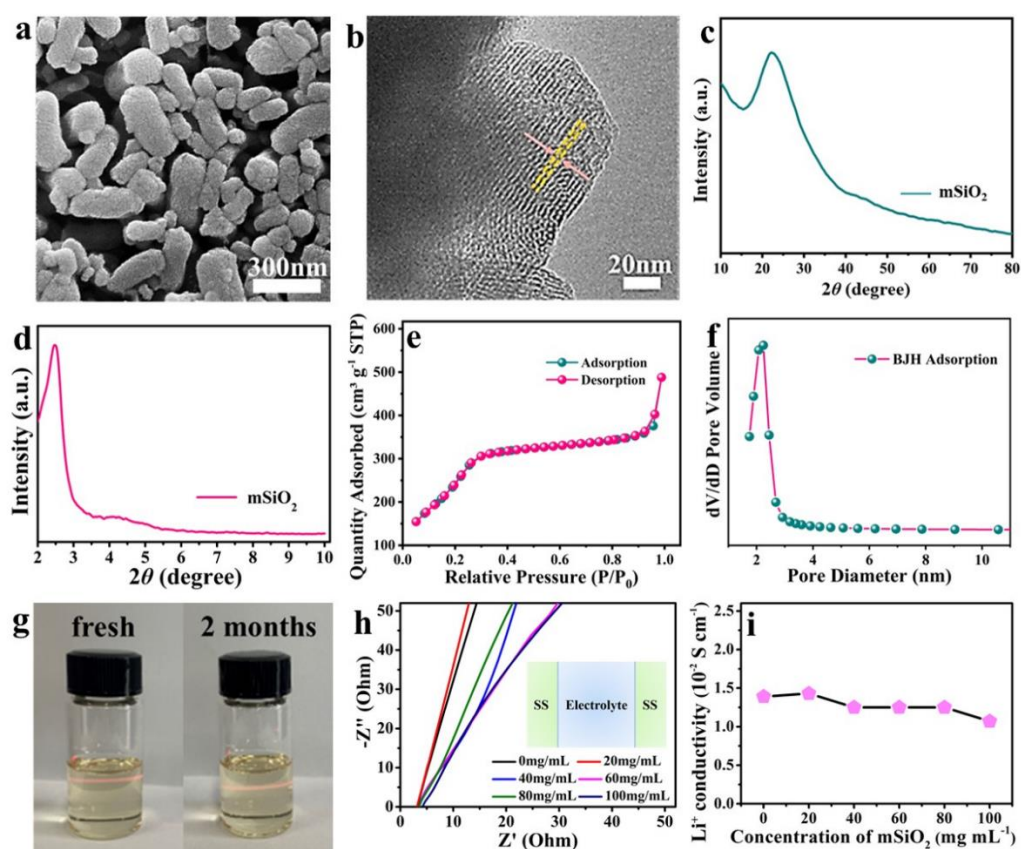
### 194 **3. Results and Discussion**

#### 195 **3.1 mSiO<sub>2</sub> and colloidal electrolytes**

196 Fig.1a is the SEM image of as-synthesized mSiO<sub>2</sub> particles, which mainly appear in the shape  
197 of ellipsoids. Fig.S1 further shows the size distribution of mSiO<sub>2</sub> particles by the long axis length,



198 an average size of  $200 \pm 10$  nm ( $N = 120$ ). Fig.1b displays the high-resolution TEM image, in which  
 199 the as-synthesized mSiO<sub>2</sub> particle exhibits close-packed hexagonal alignment of the pores. XRD  
 200 analysis in Fig.1c further confirms the presence of amorphous SiO<sub>2</sub> by the characteristic shoulder at  
 201 around  $23^\circ$  [44], and the two peaks at  $2^\circ$  to  $3^\circ$  and  $4^\circ$  to  $5^\circ$  in the small-angle XRD analysis (Fig.1d)  
 202 demonstrates the hexagonal alignment of mesopores [45]. Fig.1e displays a typical type IV isotherm  
 203 in the nitrogen adsorption/desorption test, indicative of the mesoporous structure [46,47], and the BJH  
 204 model shown in Fig.1f calculates an average pore size of  $\sim 3.34$  nm. The BET specific surface area  
 205 and pore volume are obtained as  $1016.30$  m<sup>2</sup> g<sup>-1</sup> and  $0.73$  cm<sup>3</sup> g<sup>-1</sup>, respectively.



206  
 207 **Fig. 1** (a) SEM and (b) TEM images of as-synthesized mSiO<sub>2</sub>; (c) XRD analysis of mSiO<sub>2</sub>, (d)  
 208 small-angle XRD analysis; (e) nitrogen adsorption/desorption isotherm of mSiO<sub>2</sub>; (f) BJH-  
 209 adsorption model analysis; (g) Snapshots of fresh (left) and 2-month aged (right) mSiO<sub>2</sub> colloidal  
 210 electrolyte; (h) EIS analysis of mSiO<sub>2</sub> colloidal electrolytes and (i) Li<sup>+</sup> conductivity vs. mSiO<sub>2</sub>  
 211 content.

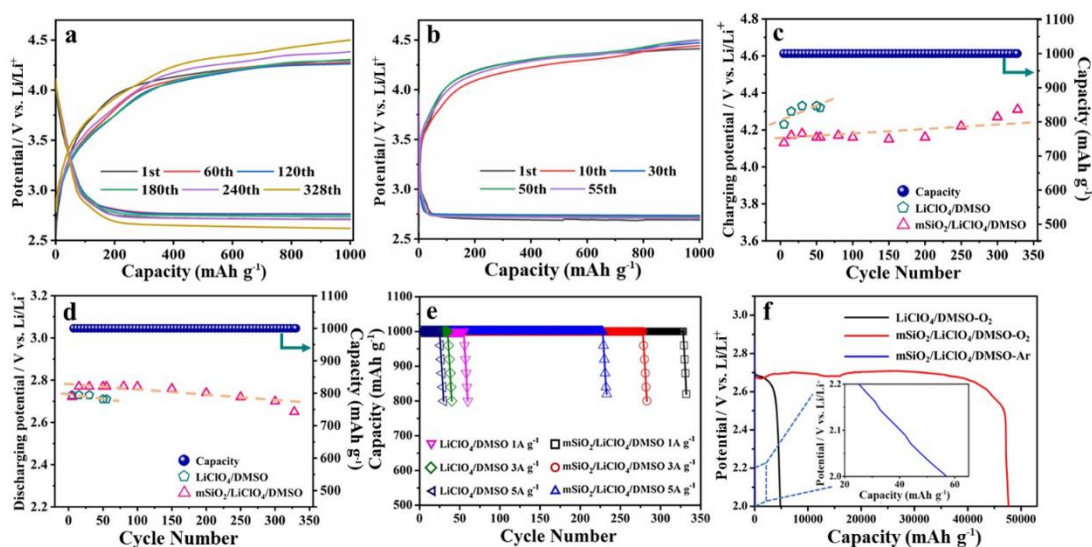
212 Fig.1g compares the freshly prepared mSiO<sub>2</sub>/LiClO<sub>4</sub>/DMSO electrolyte ( $80$  mg mL<sup>-1</sup> of  
 213 mSiO<sub>2</sub>) and an aged electrolyte (stored for 2 months). Tyndall effect can be observed for both,  
 214 where a scattering of incident lights (red) is visible because of the suspended mSiO<sub>2</sub> nanoparticles  
 215 in both electrolytes. No precipitate can be found for the aged sample, indicating the colloidal

216 electrolyte has good stability. The suspensibility of  $\text{mSiO}_2$  nanoparticles in the electrolytes was  
217 examined by centrifuging at 1200 rpm for 5 min. As depicted in Fig.S3, colloidal electrolytes with  
218 different  $\text{mSiO}_2$  contents in the 1.0 M  $\text{LiClO}_4/\text{DMSO}$  solutions have no visible change, except for  
219 the densest  $\text{mSiO}_2/\text{LiClO}_4/\text{DMSO}$  electrolyte ( $100 \text{ mg mL}^{-1}$ ) which precipitates are visible after  
220 centrifuging.

221 The ionic conductivity of  $\text{mSiO}_2/\text{LiClO}_4/\text{DMSO}$  electrolytes with different contents of  $\text{mSiO}_2$   
222 was assessed using SS|SS symmetrical cells. EIS analysis in Fig.1h-1i indicates that the introduction  
223 of  $\text{mSiO}_2$  led to a slight decrease in ionic conductivity, where the conductivity just declined from  
224  $1.39 \times 10^{-2} \text{ S cm}^{-1}$  (without  $\text{mSiO}_2$ ) to  $1.07 \times 10^{-2} \text{ S cm}^{-1}$  (with  $100 \text{ mg mL}^{-1}$  of  $\text{mSiO}_2$ ), and therefore  
225 cannot bring with an apparent increase of internal resistance. Fig.S4 shows the electrolyte prepared  
226 using commercial solid silica ( $\text{sSiO}_2$ ) and microporous Permutit as additive to the 1 M  
227  $\text{LiClO}_4/\text{DMSO}$ . It can be seen in Fig.S4c that their ionic conductivity at a concentration of  $80 \text{ mg}$   
228  $\text{mL}^{-1}$  are  $1.56 \times 10^{-2} \text{ S cm}^{-1}$  ( $\text{sSiO}_2$ ),  $1.75 \times 10^{-2} \text{ S cm}^{-1}$  (Permutit) respectively. Meanwhile at the same  
229 concentration, the ionic conductivity of  $\text{mSiO}_2/\text{LiClO}_4/\text{DMSO}$  electrolyte is  $1.25 \times 10^{-2} \text{ S cm}^{-1}$  which  
230 ensures the normal operation of battery at room temperature.

### 231 3.2 LOBs with $\text{mSiO}_2$ colloidal electrolytes

232 Battery cycle life tests are performed to indicate the stability of electrolyte or the protective effect  
233 of  $\text{mSiO}_2$  colloidal electrolyte. Fig.2a shows the cycle number of LOB using colloidal  
234  $\text{mSiO}_2/\text{LiClO}_4/\text{DMSO}$  electrolyte (with  $80 \text{ mg mL}^{-1}$  of  $\text{mSiO}_2$ ) reached 328 rounds which is more  
235 than 6 times than the one using  $1.0 \text{ mol L}^{-1}$   $\text{LiClO}_4/\text{DMSO}$  electrolyte (i.e.,  $\text{LiClO}_4/\text{DMSO}$ ) only,  
236 Fig.2b shows that the LOB with  $1.0 \text{ mol L}^{-1}$   $\text{LiClO}_4/\text{DMSO}$  electrolyte (i.e.,  $\text{LiClO}_4/\text{DMSO}$ ) can  
237 only operate for 55 cycles. Fig.S5a displays that the LOB with  $1.0 \text{ mol L}^{-1}$   $\text{sSiO}_2/\text{LiClO}_4/\text{DMSO}$   
238 electrolyte ( $80 \text{ mg mL}^{-1}$  of  $\text{sSiO}_2$ ) can only operate for 99 cycles. Fig.S5b displays that the LOB  
239 with  $1.0 \text{ mol L}^{-1}$  Permutit/ $\text{LiClO}_4/\text{DMSO}$  electrolyte (with  $80 \text{ mg mL}^{-1}$  of Permutit) can operate for  
240 187 cycles, the existence of mesopores effectively improved the cycle performance. Fig.2c-2d



241

242 **Fig. 2** Characteristics of LOBs: (a) cyclability with the  $m\text{SiO}_2/\text{LiClO}_4/\text{DMSO}$  electrolyte; (b)  
 243 cyclability with the  $\text{LiClO}_4/\text{DMSO}$  electrolyte; (c) terminal charge potentials; (d) discharge  
 244 potentials; (e) rate performance; (f) full discharge capacity, inset: enlarged curve in the  
 245  $m\text{SiO}_2/\text{LiClO}_4/\text{DMSO}$  electrolyte in argon atmosphere.

246

247 **show** that the cell with colloidal  $m\text{SiO}_2/\text{LiClO}_4/\text{DMSO}$  electrolyte has lower charge potentials and  
 248 higher discharge potentials than the one with the ordinary  $\text{LiClO}_4/\text{DMSO}$  electrolyte, hence  
 249 extending the cycle life of the LOB (the charge/discharge potential for the cell with  
 250  $m\text{SiO}_2/\text{LiClO}_4/\text{DMSO}$  electrolyte are 4.24V/2.73V, 4.31V/2.73V, 4.31V/2.75V, 4.28V/2.76V,  
 251 4.27V/2.76V, 4.28V/2.76V, 4.31V/2.74V, 4.45V/2.66V, 4.45V/2.62V for 1<sup>st</sup>, 10<sup>th</sup>, 20<sup>th</sup>, 40<sup>th</sup>, 55<sup>th</sup>,  
 252 100<sup>th</sup>, 200<sup>th</sup>, 300<sup>th</sup>, 328<sup>th</sup> cycles, respectively, the charge/discharge potential for the cell with  
 253  $\text{LiClO}_4/\text{DMSO}$  electrolyte are 4.42V/2.55V, 4.45V/2.72V, 4.48V/2.73V, 4.49V/2.72V, 4.5V/2.71V  
 254 for 1<sup>st</sup>, 10<sup>th</sup>, 20<sup>th</sup>, 40<sup>th</sup>, 55<sup>th</sup> cycles, respectively).

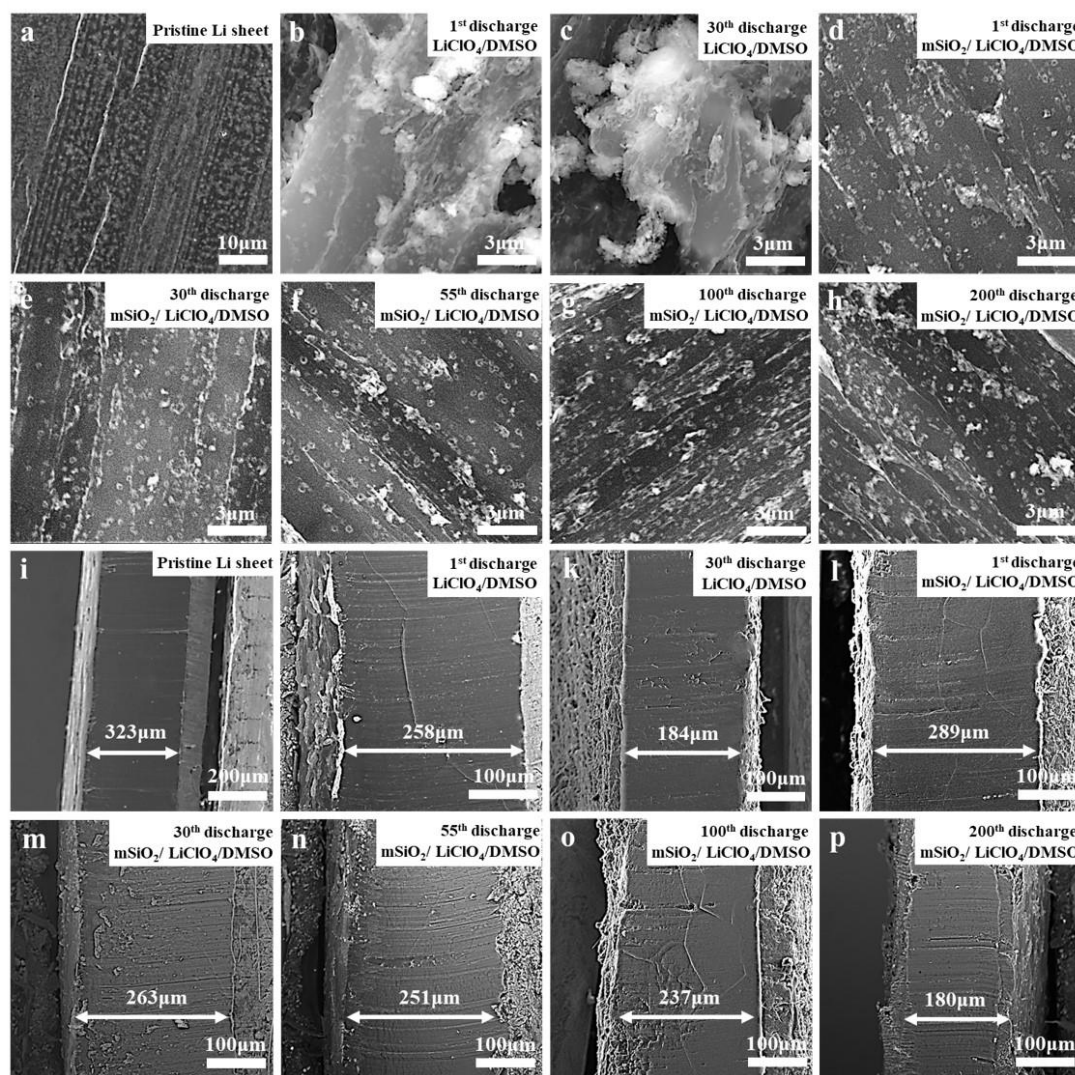
255 We also investigated the optimum  $m\text{SiO}_2$  concentration, **Fig.S2 shows** the relationship between  
 256 the concentration of  $m\text{SiO}_2$  in electrolyte and the number of battery cycles. This shows that the LOB  
 257 has the longest cycle life when the concentration of  $m\text{SiO}_2$  is 80  $\text{mg mL}^{-1}$  in  $\text{LiClO}_4/\text{DMSO}$   
 258 electrolyte. The further increase of  $m\text{SiO}_2$  concentration leads to a sharp shortening of cycle life.  
 259 The suspension test results **in Fig. S3 confirm this finding**. It can be seen that after centrifugation at  
 260 1200 rpm for 5 minutes, the electrolyte containing 100  $\text{mg mL}^{-1}$   $m\text{SiO}_2$  precipitates. Table S1 shows  
 261 the comparison of the cycle performance, charge/discharge performance and full discharge  
 262 performance of LOBs made of electrolytes with three different additives.  $m\text{SiO}_2/\text{LiClO}_4/\text{DMSO}$

263 electrolyte shows a lower cycle life and comparable rate performance to the others, but the full  
264 discharge performance is clearly higher than the LOBs with Au/LiClO<sub>4</sub>/DMSO and  
265 Ag/LiClO<sub>4</sub>/DMSO electrolyte, it shows that the existence of mesoporous silica channels provides a  
266 transport channel for oxygen and Li<sup>+</sup>, improves the mass transfer, avoids premature passivation of  
267 the cathode, and thus increases the capacity. Fig. 2e shows the rate performance the LOB with the  
268 LiClO<sub>4</sub>/DMSO electrolyte only presents 35 and 25 cycles at the current densities of 3 A g<sup>-1</sup> and 5 A  
269 g<sup>-1</sup>, while the corresponding values are increased to 278 and 228 rounds for the cell with  
270 mSiO<sub>2</sub>/LiClO<sub>4</sub>/DMSO colloidal electrolyte, respectively, which are more than 7-fold longer than  
271 the cell with the LiClO<sub>4</sub>/DMSO electrolyte at the high charge/discharge rates. Fig.S5c shows that  
272 the LOBs with sSiO<sub>2</sub>/LiClO<sub>4</sub>/DMSO electrolyte can only operate 49 and 36 cycles at the  
273 charge/discharge current densities of 3 A g<sup>-1</sup> and 5 A g<sup>-1</sup>, respectively and the LOBs with the  
274 Permutit/LiClO<sub>4</sub>/DMSO electrolyte present 91 and 60 cycles that are much lower than the LOBs  
275 with colloidal mSiO<sub>2</sub>/LiClO<sub>4</sub>/DMSO electrolyte.

276 Moreover, the full-discharge capacity for the cell with LiClO<sub>4</sub>/DMSO electrolyte is tested as  
277 4800 mAh, and the one with the mSiO<sub>2</sub>/LiClO<sub>4</sub>/DMSO colloidal electrolyte reaches up to 47600  
278 mAh, which is one magnitude higher. The full-discharge capacity in argon atmosphere was tested  
279 for only 57 mAh as shown in the inset, suggesting that the large capacity is attributed to the ORR  
280 process. Fig.S5d further displays the full-discharge capacity of LOBs where the capacity in the LOB  
281 with sSiO<sub>2</sub>/LiClO<sub>4</sub>/DMSO electrolyte is tested as 8922 mAh, and the one with Permutit/  
282 LiClO<sub>4</sub>/DMSO electrolyte is 18312 mAh. In general, the LOB with mSiO<sub>2</sub>/LiClO<sub>4</sub>/DMSO  
283 electrolyte shows significant improvements in battery cycle stability, rate performance, and full-  
284 discharge capacity compared to the LOBs with LiClO<sub>4</sub>/DMSO, sSiO<sub>2</sub>/LiClO<sub>4</sub>/DMSO, and the  
285 Permutit/LiClO<sub>4</sub>/DMSO electrolytes. This suggest that the colloidal electrolyte accelerates the  
286 cathode process, more discharge product is allowed to form in the cell with the colloidal electrolyte.

287 The characterizations of morphology and thickness of Li anodes before and after cyclability  
288 testing are performed. Fig.3a shows a compact and smooth look of the surface of pristine Li anode,  
289 with a thickness of 323 μm (Fig.3i). After the 1<sup>st</sup> discharge in the cell with the LiClO<sub>4</sub>/DMSO  
290 electrolyte, the surface of Li anode becomes rougher as shown in Fig.3b, its thickness is also reduced  
291 to 258 μm in Fig.3j, After the 30<sup>th</sup> discharge in the cell with the LiClO<sub>4</sub>/DMSO electrolyte, the  
292 surface of Li anode surface becomes rougher as shown in Fig.3c, its thickness is also decreased to

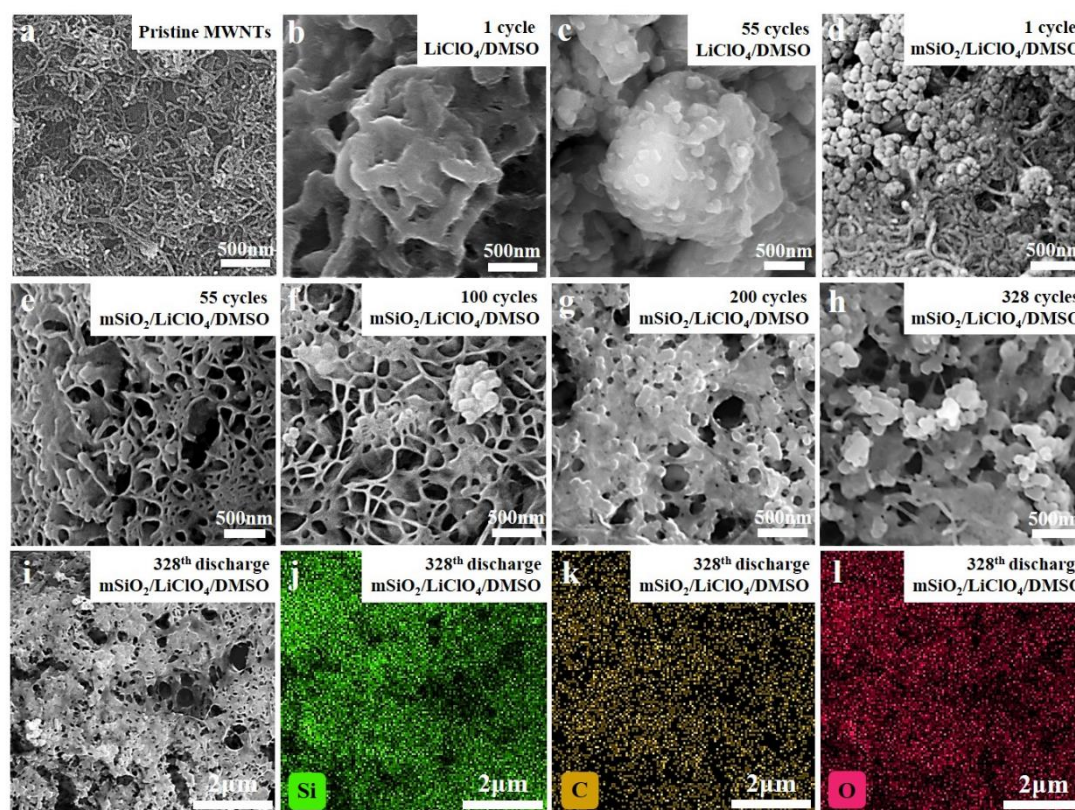
293 184  $\mu\text{m}$  in Fig.3k. After cycling 55 times, the Li anode was totally pulverized (Fig.S6a). In contrast,  
 294 the Li surface maintains rather smooth after the 1<sup>st</sup> discharge in the LOB with  $\text{mSiO}_2/\text{LiClO}_4/\text{DMSO}$   
 295 electrolyte (Fig.3d), and the residual Li thickness retains at 289  $\mu\text{m}$  shown in Fig.3l. Fig.3e-h shows  
 296 flat and smooth anode surface after 30, 55, 100, 200 cycles, and the thickness decreased to 263, 251,  
 297 237, 180  $\mu\text{m}$  accordingly (Fig.3m-3p). At the 328<sup>th</sup> cycle, the Li anode completely vanished  
 298 (Fig.S6b). Fig.S7 compares the composition of pulverized anode powders in the  $\text{LiClO}_4/\text{DMSO}$



299  
 300 **Fig. 3** Morphology and thickness of Li anodes in the LOBs: (a, i) pristine Li anode; (b, j) after the  
 301 1<sup>st</sup> discharge with the 1.0 M  $\text{LiClO}_4/\text{DMSO}$  electrolyte; (c, k) after the 30<sup>th</sup> discharge with the 1.0 M  
 302  $\text{LiClO}_4/\text{DMSO}$  electrolyte; (d, l) after the 1<sup>st</sup> discharge in the  $\text{mSiO}_2/\text{LiClO}_4/\text{DMSO}$  electrolyte (80  
 303  $\text{mg mL}^{-1}$ ); (e, m) after the 30<sup>th</sup> discharge in the cell with  $\text{mSiO}_2/\text{LiClO}_4/\text{DMSO}$  colloidal electrolyte  
 304 (80  $\text{mg mL}^{-1}$ ); (f, n) after the 1<sup>st</sup> discharge in the  $\text{mSiO}_2/\text{LiClO}_4/\text{DMSO}$  electrolyte (80  $\text{mg mL}^{-1}$ ); (g,  
 305 o) after the 1<sup>st</sup> discharge in the  $\text{mSiO}_2/\text{LiClO}_4/\text{DMSO}$  electrolyte (80  $\text{mg mL}^{-1}$ ); (h, p) after the 1<sup>st</sup>  
 306 discharge in the  $\text{mSiO}_2/\text{LiClO}_4/\text{DMSO}$  electrolyte (80  $\text{mg mL}^{-1}$ ).  
 307 (after 55 cycles) and  $\text{mSiO}_2/\text{LiClO}_4/\text{DMSO}$  electrolytes (after 328 cycles), both assigned to  $\text{LiOH}$

308 according to XRD analysis. This result suggests that the mSiO<sub>2</sub> colloidal electrolyte can relieve the  
 309 corrosion of Li anode, and promote the uniform stripping/plating of Li.

310 SEM images of LOBs is shown in Figs.4a-h. Fig. 4a is the pristine electrode surface with  
 311 MWNTs completely covered on the carbon paper substrate. Fig.4b shows the cathode surface of  
 312 LOB using LiClO<sub>4</sub>/DMSO as electrolyte after 1<sup>st</sup> cycle test with undecomposed discharge product.  
 313 Fig.4c illustrates that the cathode surface is fully covered by large pieces of discharge products in  
 314 the LOB with LiClO<sub>4</sub>/DMSO electrolyte after cycling 55 times. Fig.4d shows the cathode surface  
 315 of the LOB with mSiO<sub>2</sub>/ LiClO<sub>4</sub>/DMSO electrolyte after 1<sup>st</sup> cycle, the MWNTs are clearly observed,  
 316 indicating that the discharge product is decomposed. Fig. 4e-4f are images of the cathode surface of  
 317 LOB with mSiO<sub>2</sub>/ LiClO<sub>4</sub>/DMSO electrolyte after 55 and 100 cycles. No discharge product can be  
 318 observed until the one after 200 cycles in Fig. 4g. The discharge product accumulated further after



319  
 320 **Fig. 4** SEM images of the MWNTs cathodes in LOBs: (a) pristine; (b) after 1 cycle in the 1.0 M  
 321 LiClO<sub>4</sub>/DMSO electrolyte; (c) after 55 cycles in the 1.0 M LiClO<sub>4</sub>/DMSO electrolyte; (d) after 1  
 322 cycle in the 1.0 M mSiO<sub>2</sub>/LiClO<sub>4</sub>/DMSO electrolyte; (e-h) after 55, 100, 200, 300 and 328 cycles in  
 323 the mSiO<sub>2</sub>/LiClO<sub>4</sub>/DMSO colloidal electrolyte; (i~l) element mapping of the MWNTs cathode after  
 324 the 328<sup>th</sup> discharge in the mSiO<sub>2</sub>/LiClO<sub>4</sub>/DMSO colloidal electrolyte.

325 328 cycles (Fig. 4h) on the cathode, but MWNTs still appear, indicating that the suspended mSiO<sub>2</sub>

326 in the electrolyte effectively improves the reversibility of cathode reactions.

327 Elemental mapping results (Fig. 4i-4l) reveal Si (with C and O elements) in the discharge  
328 product after 328 cycles in the mSiO<sub>2</sub>/LiClO<sub>4</sub>/DMSO electrolyte, indicating that the suspended  
329 mSiO<sub>2</sub> nanoparticles are co-deposited with the discharge product at the cathode. We further verify  
330 the co-deposition during the cycling of battery, The elemental mapping analysis of cathode surface  
331 with mSiO<sub>2</sub>/LiClO<sub>4</sub>/DMSO colloidal electrolyte after the 1<sup>st</sup> and 55<sup>th</sup> discharges are summarized in  
332 Fig. S8 (a-d) and (e-h), with the cross-sectional elemental mapping analysis of these cathodes after  
333 the 1<sup>st</sup>, 55<sup>th</sup> and 328<sup>th</sup> discharge shown in (i-l), (m-p) and (q-t). It is concluded that the co-deposition  
334 of mSiO<sub>2</sub> and discharge products on the cathode exists in the whole cycle.

335 LiOH sedimentation was found on the separator material during LOBs cycling. In comparison  
336 to the pristine glass fibre separator (Fig.S9a), a minor amount of deposits can be observed after the  
337 1<sup>st</sup> discharge (Fig.S9b) and 1<sup>st</sup> recharge (Fig.S9c) in the LOB using LiClO<sub>4</sub>/DMSO electrolyte. Most  
338 of the separator has been covered by the deposit after the 55<sup>th</sup> discharge (Fig.S9d). In contrast,  
339 sedimentation can hardly be seen on the separator after the 1<sup>st</sup> discharge (Fig. S9e) and 1<sup>st</sup> recharge  
340 (Fig.S9f) for mSiO<sub>2</sub>/LiClO<sub>4</sub>/DMSO electrolyte LOB, after the 55<sup>th</sup> cycle there is little can be seen  
341 (Fig.S9 g-h), even after the 100<sup>th</sup>, 150<sup>th</sup>, 200<sup>th</sup> cycles there also little can be found (Fig.S9 i-n) until  
342 the 300<sup>th</sup> cycle, some deposits can be observed (Fig.S9o) and even at the 328<sup>th</sup> cycle (Fig.S9p) . In  
343 Fig.S10, XRD analysis of the deposits indicates that the composition of sediment is determined as  
344 LiOH. The colloidal electrolyte effectively suppresses the side reactions in electrolyte. The  
345 existence of mSiO<sub>2</sub> particles can promote the reversibility of positive and negative pole cycles and  
346 reduce the accumulation of by-products. Due to the existence of pores, some charge/discharge  
347 intermediates (such as O<sub>2</sub><sup>-</sup>, LiO<sub>2</sub>) and trace water can be adsorbed, so that the side reactions caused  
348 by polarization or external environment can be reduced, enabling a long operating time for battery.

349

### 350 3.3 Effect of mSiO<sub>2</sub> on battery reactions

351 Li|Li symmetric cells were utilized to analyze the anode reactions in the LiClO<sub>4</sub>/DMSO and  
352 mSiO<sub>2</sub>/LiClO<sub>4</sub>/DMSO electrolytes, at a current density of 0.1 mA cm<sup>-2</sup> with a limited capacity of  
353 0.1 mAh cm<sup>-2</sup>. In Fig.5a, it is found that the cell with LiClO<sub>4</sub>/DMSO electrolyte (green) begins with  
354 a voltage gap of 102 mV, which rapidly expands to 939 mV after 238 h. However, the voltage gap  
355 in mSiO<sub>2</sub>/LiClO<sub>4</sub>/DMSO electrolyte (red) starts at 30 mV, and remains at 35mV after 238 h. After

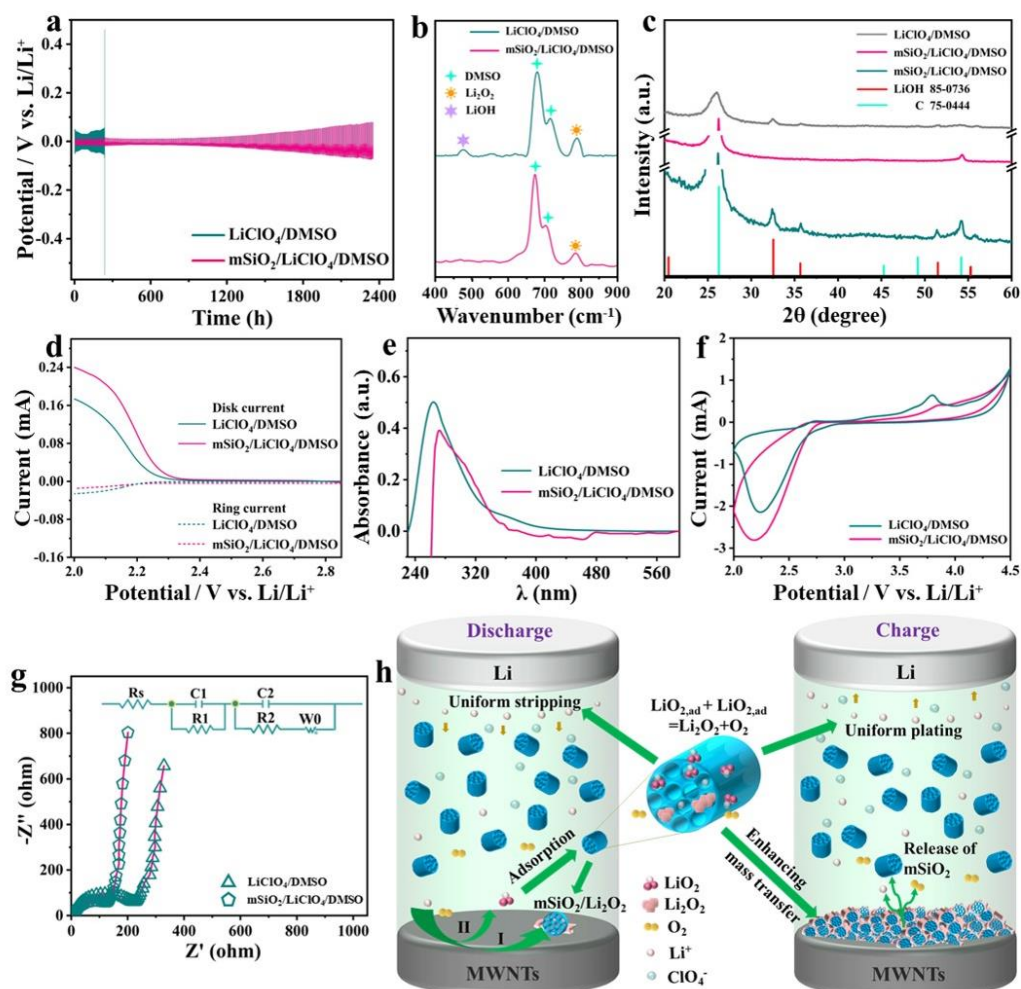
356 cycling for 2300 h, the gap stays as low as 149 mV, demonstrating an improved stripping/plating of  
357 Li. This agrees with the report from Kim *et al* that the Li<sup>+</sup> solvation environment can be modified  
358 by the interaction between Li<sup>+</sup> and suspended Li<sub>2</sub>O, leading to homogenised Li<sup>+</sup> flux at the Li anode  
359 [39]. Perez-Beltran *et al* also suggested that lithiation can also occur at the surface of SiO<sub>2</sub> via the  
360 breakage of Si-O bonds at a Li/Si ratio of 3.48 [48]. The suspended mSiO<sub>2</sub> with large specific surface  
361 area in the electrolyte can adjust the Li<sup>+</sup> flux by the interaction between mSiO<sub>2</sub> and Li<sup>+</sup>, leading to  
362 the uniform plating/stripping of Li.

363 We next study the cathode reactions by Raman analysis. Two peaks at 670 cm<sup>-1</sup> and 695 cm<sup>-1</sup>  
364 are found in both products after the 1<sup>st</sup> discharge as displayed in Fig.5b, which are assigned to the  
365 organic solvent DMSO. Besides, the spectrum in the LiClO<sub>4</sub>/DMSO electrolyte (cyan line) displays  
366 two more peaks at around 485 cm<sup>-1</sup> and 785 cm<sup>-1</sup> assigned to LiOH and Li<sub>2</sub>O<sub>2</sub> [49,50], respectively;  
367 while in the mSiO<sub>2</sub>/LiClO<sub>4</sub>/DMSO electrolyte (pink line), there is only one peak at 785 cm<sup>-1</sup>,  
368 attributed to the major discharge product Li<sub>2</sub>O<sub>2</sub>. Fig.S11 shows the XRD analysis of discharge  
369 products in the LOBs with LiClO<sub>4</sub>/DMSO (grey) at the 40<sup>th</sup> discharge and with  
370 mSiO<sub>2</sub>/LiClO<sub>4</sub>/DMSO at the 300<sup>th</sup> (pink) discharge, peaks of LiOH and Li<sub>2</sub>O<sub>2</sub> co-exist. XRD  
371 analysis in Fig.5c further indicates that the content of Li<sub>2</sub>O<sub>2</sub> decreases with battery cycling in the  
372 LiClO<sub>4</sub>/DMSO electrolyte (grey line), and the major discharge product basically becomes LiOH at  
373 the 55<sup>th</sup> discharge. In mSiO<sub>2</sub>/LiClO<sub>4</sub>/DMSO electrolyte (pink line), we can barely trace LiOH on  
374 the cathode at the 55<sup>th</sup> discharge, but it becomes the major product after 328 cycles (green line). The  
375 result demonstrates that the presence of mSiO<sub>2</sub> in the electrolyte is in favour of forming Li<sub>2</sub>O<sub>2</sub>, and  
376 therefore improves the reversibility of cathode reactions.

377 To understand these results, rotating ring-disc electrode (RRDE) analysis was carried out, in  
378 which the ring current associated to the oxidation of ORR intermediates (LiO<sub>2</sub> or O<sub>2</sub><sup>-</sup>)<sup>[51]</sup>, the use of  
379 Ag/AgNO<sub>3</sub> reference electrode <sup>[52]</sup>. The disk current become larger (Fig.5d) and the ring current is  
380 smaller in the mSiO<sub>2</sub>/LiClO<sub>4</sub>/DMSO electrolyte (pink lines) than those in the LiClO<sub>4</sub>/DMSO  
381 electrolyte (cyan lines), showing that the content of ORR intermediates in the electrolyte is  
382 suppressed by mSiO<sub>2</sub>. The contents of ORR intermediates in LiClO<sub>4</sub>/DMSO and  
383 mSiO<sub>2</sub>/LiClO<sub>4</sub>/DMSO electrolytes (V = 10 mL) were monitored by UV-vis spectra. Fig.5e  
384 illustrates that the absorbance at λ = 260 nm (characteristic absorbance)<sup>[53]</sup> in the  
385 mSiO<sub>2</sub>/LiClO<sub>4</sub>/DMSO electrolyte, which is clearly lower than the one with LiClO<sub>4</sub>/DMSO



386 electrolyte, indicative of lower content of peroxide the presence of suspended mSiO<sub>2</sub>. This prove  
 387 that the ORR intermediates LiO<sub>2</sub> or O<sub>2</sub><sup>-</sup> can be adsorbed by the suspended mSiO<sub>2</sub> when they diffuse  
 388 into the electrolyte and then are converted to Li<sub>2</sub>O<sub>2</sub> by disproportionation<sup>[41]</sup>. Consequently, the  
 389 cleavage of electrolyte and corrosion of Li anode are inhibited.



390  
 391 **Fig.5** LOBs with the 1.0 M LiClO<sub>4</sub>/DMSO and mSiO<sub>2</sub>/LiClO<sub>4</sub>/DMSO (80 mg mL<sup>-1</sup>) electrolytes: (a)  
 392 Li|Li symmetrical cells; (b) Raman analysis of the discharge products at the 1<sup>st</sup> discharge; (c) XRD  
 393 analysis of the cathode product in the LiClO<sub>4</sub>/DMSO electrolyte (grey) at the 55<sup>th</sup> discharge, and  
 394 the products in mSiO<sub>2</sub>/LiClO<sub>4</sub>/DMSO electrolyte at the 55<sup>th</sup> (pink) and 328<sup>th</sup> (blue) discharges; (d)  
 395 RRDE analysis; (e) UV-vis analysis of ORR intermediates ( $\lambda=260$  nm) in the LiClO<sub>4</sub>/DMSO (blue)  
 396 and mSiO<sub>2</sub>/LiClO<sub>4</sub>/DMSO (pink) electrolytes; (f) cyclic voltammograms; (g) EIS analysis of the  
 397 LOBs after the 1<sup>st</sup> discharge; (h) **Illustration** for the effect of suspended mSiO<sub>2</sub> in battery reaction.

398 Moreover, the significant enhancement in rate performance and full discharge capacity of  
 399 LOBs closely associated with the co-deposition of mSiO<sub>2</sub> and Li<sub>2</sub>O<sub>2</sub> (ref. Fig.4i ~ 4l). Cyclic  
 400 voltammetric analysis (Fig.5f) illustrates that the ORR peak current (cyan line) in mSiO<sub>2</sub>/LiClO<sub>4</sub>/  
 401 DMSO electrolyte is measured as 2.81mA, on the contrary, the one with the absence of inorganic

402 additive (pink line) shows a result of 2.14 mA, which suggests that the incorporation with mSiO<sub>2</sub>  
403 improves the ORR kinetics and allows more Li<sub>2</sub>O<sub>2</sub> loading at the cathode. In addition, the analysis  
404 of electrochemical impedance spectroscopy (EIS) of the LOBs after the 1<sup>st</sup> discharge also displays  
405 the apparent influence of mSiO<sub>2</sub> in electrolyte. In Fig.5g, the LOB with the LiClO<sub>4</sub>/DMSO  
406 electrolyte exhibits an impedance of 219 Ω, and the one in the mSiO<sub>2</sub>/LiClO<sub>4</sub>/DMSO exhibits a  
407 much smaller impedance of 121 Ω. Considering the ignorable change at anode and in electrolyte  
408 after the 1<sup>st</sup> discharge, the different impedance can be attributed to improve electric conductivity at  
409 the cathode. Fig.S12a displays the cyclic voltammograms of sSiO<sub>2</sub>/LiClO<sub>4</sub>/DMSO (grey line) and  
410 Permutit/LiClO<sub>4</sub>/DMSO electrolyte (red line), the increase in ORR peak intensity further evidenced  
411 the existence of mesopores. The LOB with mSiO<sub>2</sub> colloidal electrolyte also exhibits a smaller  
412 impedance than the other two, as shown in Fig.S12b, the LOBs with sSiO<sub>2</sub>/LiClO<sub>4</sub>/DMSO (black  
413 line) and Permutit/LiClO<sub>4</sub>/DMSO electrolyte (red line) after the 1<sup>st</sup> discharge show higher  
414 impedance values. The mesoporous structure and hydrophilic surface of mSiO<sub>2</sub> prompt the transfer  
415 of Li<sup>+</sup> and O<sub>2</sub>, and therefore effectively enhances the mass transfer in discharge product, lead to a  
416 reduction of electric conductivity at the cathode and the decrease of charging potentials of LOBs.

417 As illustrated in Fig.5h, the suspended mSiO<sub>2</sub> in electrolyte enhance LOBs through three  
418 aspects: (1) *Inhibiting side reactions*. The suspended mSiO<sub>2</sub> can reduce the content of superoxide  
419 intermediates in the electrolyte with its large specific surface area and increases the content of Li<sub>2</sub>O<sub>2</sub>  
420 in the discharge product. This prevents the electrolyte from decomposition and the Li anode from  
421 corrosion during battery cycling. The adsorption is also in favour of increasing the capacity of LOBs  
422 by enhancing the solution-growth of Li<sub>2</sub>O<sub>2</sub>. (2) *Improving mass transfer at the cathode*. The co-  
423 deposited mSiO<sub>2</sub> assists in transferring Li<sup>+</sup> and O<sub>2</sub> by its mesopores in discharge/charge cycles and  
424 reduces the charging overpotential in the OER process. The incorporated mSiO<sub>2</sub> can be released  
425 into the electrolyte by decomposing Li<sub>2</sub>O<sub>2</sub>. (3) *Homogenising the stripping/plating of Li*. The  
426 suspended mSiO<sub>2</sub> in electrolyte can modify the Li<sup>+</sup> solvation environment based on the interaction  
427 with Li<sup>+</sup>, which results in uniform Li<sup>+</sup> flux and suppresses the dendritic growth of Li during cycling.

#### 428 **4. Conclusion**

429 We describe an approach to achieve high performance LOBs by using a stable colloidal  
430 electrolyte containing mSiO<sub>2</sub> with a well-ordered hexagonal mesoporous structure (a BET specific  
431 surface area of 1016.30 m<sup>2</sup> g<sup>-1</sup>). The cycle life has been extended from 55 rounds in the conventional

432 LiClO<sub>4</sub>/DMSO electrolyte to 328 rounds with 80 mg L<sup>-1</sup> of colloidal mSiO<sub>2</sub> in the electrolyte. The  
433 explicit enhancements are shown in rate performance and full-discharge capacity. Morphological  
434 and electrochemical analyses prove that the suspended mSiO<sub>2</sub> in the electrolyte exerts a synergistic  
435 effect on both anode and cathode. At the anode, the presence of mSiO<sub>2</sub> optimised the  
436 stripping/plating processes of Li by homogenising Li<sup>+</sup> flux. At the cathode, the suspended mSiO<sub>2</sub>  
437 adsorbs the superoxide intermediates in electrolyte with its large specific surface area, and co-  
438 deposits with Li<sub>2</sub>O<sub>2</sub> in discharging, thus improves the mass transfer through its mesopores for the  
439 decomposition of Li<sub>2</sub>O<sub>2</sub> during charging process. Hence, the electrolyte and Li anode are protected  
440 from oxidative cleavage and corrosion, and the decomposition of Li<sub>2</sub>O<sub>2</sub> was largely accelerated. We  
441 hope this approach to open a window for suppressing side reactions with mesoporous colloids in  
442 non-aqueous electrolytes, to encompass new route for future Li-ion batteries.

443

#### 444 **Acknowledgement**

445 The authors appreciate the financial support from the National Natural Science Foundation of  
446 China (No. 51874051, 52111530139), Jiangsu Specially-Appointed Professor Fund by Jiangsu  
447 Education Department, Science and Technology Plan Project of Changzhou (No.  
448 CQ20D2EHFA034), the UK Engineering Physics and Science Research Council (Grant No.  
449 EP/S032886/1), Guangxi Natural Science Foundation (No. 2019GXNSFAA245046).

450

451

452 **Reference**

- 453 [1] J. Zhang, X. Chen, Y. Lei, H. Lu, J. Xu, S. Wang, M. Yan, F. Xiao, J. Xu, Highly rechargeable  
454 lithium oxygen batteries cathode based on boron and nitrogen co-doped holey graphene, Chem.  
455 Eng. J. 428 (2022) 131025.
- 456 [2] W. Zhang, S. Tang, Z. Chen, X. Xiong, B. Chen, K. Wu, G. Xu, S. Cheng, Y. Cao, The  
457 controllable construction of nanochannel in two-dimensional lamellar film for efficient oxygen  
458 reduction reaction and lithium-oxygen batteries, Chem. Eng. J. 430 (2022) 132489.
- 459 [3] Y.J. Oh, J. H. Kim, S. K. Park, J. S. Park, J. K. Lee, Y. Kang, Highly Efficient Hierarchical  
460 Multiroom-Structured Molybdenum Carbide/Carbon Composite Microspheres Grafted with  
461 Nickel-Nanoparticle-Embedded Nitrogen-Doped Carbon Nanotubes as Air Electrode for  
462 Lithium-Oxygen Batteries, Chem. Eng. J. 351 (2018) 886-896.
- 463 [4] J. Gao, X. Cai, J. Wang, M. Hou, L. Lai, L.L. Zhang, Recent progress in hierarchically  
464 structured O<sub>2</sub>-cathodes for Li-O<sub>2</sub> batteries, Chem. Eng. J 352 (2018) 972-995.
- 465 [5] M.-G. Jeong, W.-J. Kwak, J.Y. Kim, J.K. Lee, Y.-K. Sun, H.-G. Jung, Uniformly distributed  
466 reaction by 3D host-lithium composite anode for high rate capability and reversibility of Li-  
467 O<sub>2</sub> batteries, Chem. Eng. J 427 (2022) 130914.
- 468 [6] H. Hou, Y. Cong, Q. Zhu, Z. Geng, X. Wang, Z. Shao, X. Wu, K. Huang, S. Feng, Fluorine  
469 induced surface reconstruction of perovskite ferrite oxide as cathode catalyst for prolong-life  
470 Li-O<sub>2</sub> battery, Chem. Eng. J 448 (2022) 137684.
- 471 [7] Y. Zhang, Y. Liu, J. Zhou, D. Wang, L. Tan, C. Yi, 3D cubic framework of fluoride perovskite  
472 SEI inducing uniform lithium deposition for air-stable and dendrite-free lithium metal anodes,  
473 Chem. Eng. J, 431 (2022) 134266.
- 474 [8] L. Wei, N. Deng, J. Ju, J. Kang, X. Wang, L. Ding, W. Kang, B. Cheng, A review on nanofiber  
475 materials for lithium-metal batteries to suppress the dendritic lithium growth, Chem. Eng. J,  
476 433 (2022) 134392.
- 477 [9] B. Liu, M. Du, B. Chen, Y. Zhong, J. Zhou, F. Ye, K. Liao, W. Zhou, C. Cao, R. Cai, Z. Shao,  
478 A simple strategy that may effectively tackle the anode-electrolyte interface issues in solid-  
479 state lithium metal batteries, Chem. Eng. J 427 (2022) 131001.
- 480 [10] K. Luo, G. Zhu, Y. Zhao, Z. Luo, X. Liu, K. Zhang, Y. Li, K. Scott, Enhanced Cycling Stability  
481 of Li-O<sub>2</sub> Batteries by Using a Polyurethane/SiO<sub>2</sub>/Glass Fiber Nanocomposite Separator, J.

482 Mater. Chem. A. 6 (2018) 7770.

483 [11] Y. Wei, H. Xu, H. Cheng, W. Guan, J. Yang, Z. Li, Y. Huang, An oxygen vacancy-rich ZnO  
484 layer on garnet electrolyte enables dendrite-free solid state lithium metal batteries, Chem. Eng.  
485 J 433 (2022) 133665.

486 [12] J.H. Kim, H.S. Woo, W.K. Kim, K.H. Ryu, D.W. Kim, Improved Cycling Performance of  
487 Lithium-Oxygen Cells by Use of a Lithium Electrode Protected with Conductive Polymer and  
488 Aluminum Fluoride, ACS Appl. Mater. Interfaces. 8 (2016) 32300-32306.

489 [13] J. Xu, Q. Liu, Y. Yu, J. Wang, J. Yan, X. Zhang, In Situ Construction of Stable Tissue-  
490 Directed/Reinforced Bifunctional Separator/Protection Film on Lithium Anode for Lithium-  
491 Oxygen Batteries, Adv. Mater. 27 (2017) 1606552-1606557.

492 [14] Z. Huang, J. Ren, W. Zhang, M. Xie, Y. Li, D. Sun, Y. Shen, Y. Huang, Protecting the Li-Metal  
493 Anode in a Li-O<sub>2</sub> Battery by using Boric Acid as an SEI-Forming Additive, Adv. Mater. 30  
494 (2018) 1803270.

495 [15] X. Zhang, Q. Zhang, X. Wang, C. Wang, Y. Chen, Z. Xie, Z. Zhou, An Extremely Simple  
496 Method for Protecting Lithium Anodes in Li-O<sub>2</sub> Batteries, Angew. Chem. Int. Ed. 57 (2018)  
497 12814-12818.

498 [16] M. Asadi, B. Sayahpour, P. Abbasi, A.T. Ngo, K. Karis, J.R. Jokisaari, C. Liu, B. Narayanan,  
499 M. Gerard, P. Yasaei, X. Hu, A. Mukherjee, K.C. Lau, R.S. Assary, F.K. Araghi, R.F. Klie, L.A.  
500 Curtiss, A.S.-Khojin, A lithium-oxygen battery with a long cycle life in an air-like atmosphere,  
501 Nature. 555 (2018) 502-506.

502 [17] Z. Luo, G. Zhu, L. Guo, F. Li, Y. Li, M. Fu, Y. Cao, Y. Li, K. Luo, Improving the cyclability  
503 and capacity of Li-O<sub>2</sub> batteries via low rate pre-activation, Chem. Commun. 55 (2019) 2094-  
504 2097.

505 [18] M. T. Rauter, M. Augustin, L. Spitthoff, A. M. Svensson, Product formation during discharge:  
506 a combined modelling and experimental study for Li-O<sub>2</sub> cathodes in LiTFSI/DMSO and  
507 LiTFSI/TEGDME electrolytes, J. Appl. Electrochem. 51 (2021) 1437-1447.

508 [19] E. Nasybulin, W. Xu, M.H. Engelhard, Z.M. Nie, S.D. Burton, L.L. Cosimbescu, M.E. Gross,  
509 J. Zhang, Effects of Electrolyte Salts on the Performance of Li-O<sub>2</sub> Batteries, J. Phys. Chem. C.  
510 117 (2013) 2635-2645.

511 [20] R. Black, S.H. Oh, J.H. Lee, T. Yim, B. Adams, L.F. Nazar, Screening for Superoxide Reactivity  
512 in Li-O<sub>2</sub> Batteries: Effect on Li<sub>2</sub>O<sub>2</sub>/LiOH Crystallization, J. Am. Chem. Soc. 134 (2012) 2902-  
513 2905.

514 [21] Z. Peng, S.A. Freunberger, Y. Chen, P.G. Bruce, A Reversible and Higher-Rate Li-O<sub>2</sub> Battery,  
515 Science. 337 (2012) 563-566.

- 516 [22] S. Ganapathy, Z. Li, M.S. Anastasaki, S. Basak, X.-F. Miao, K. Goubitz, H.W. Zandbergen,  
517 F.M. Mulder, M. Wagemaker, Use of Nano Seed Crystals To Control Peroxide Morphology in  
518 a Nonaqueous Li-O<sub>2</sub> Battery, *J. Phys. Chem. C*, 120 (2016) 18421-18427.
- 519 [23] C.H. Hwang, M.-J. Kwak, J.H. Jeong, K. Baek, K.-Y. Yoon, C.L. An, J.-W. Min, J.H. Kim, J.  
520 Lee, S. Kang, J.-H. Jang, J.-H. Jang, Critical Void Dimension of Carbon Frameworks to  
521 Accommodate Insoluble Products of Lithium-Oxygen Batteries, *ACS Appl. Mater. Interfaces*,  
522 14 (2022) 492-501.
- 523 [24] J. Li, Y. Zhao, M. Zou, C. Wu, Z. Huang, L. Guan, An Effective Integrated Design for Enhanced  
524 Cathodes of Ni Foam-Supported Pt/Carbon Nanotubes for Li-O<sub>2</sub> Batteries, *ACS Appl. Mater.*  
525 *Interfaces* 6 (2014) 12479-12485.
- 526 [25] Z. Jian, P. Liu, F. Li, P. He, X. Guo, M. Chen, H. Zhou, Core-Shell-Structured CNT@RuO<sub>2</sub>  
527 Composite as a High-Performance Cathode Catalyst for Rechargeable Li-O<sub>2</sub> Batteries, *Angew.*  
528 *Chem. Int. Ed.* 53 (2014) 442-446.
- 529 [26] C. Sun, F. Li, C. Ma, Y. Wang, Y. Ren, W. Yang, Z. Ma, J. Li, Y. Chen, Y. Kim, L. Chen,  
530 Graphene-Co<sub>3</sub>O<sub>4</sub> nanocomposite as an efficient bifunctional catalyst for lithium-air batteries  
531 *J. Mater. Chem. A*. 2 (2014) 7188-7196.
- 532 [27] J. Liu, D. Li, Y. Wang, S. Zhang, Z. Kang, H. Xie, L. Sun, MoO<sub>2</sub> nanoparticles/carbon textiles  
533 cathode for high performance flexible Li-O<sub>2</sub> battery, *J. Energy Chem.* 47 (2020) 66-71.
- 534 [28] F. Chao, B. Wang, J. Ren, Y. Lu, W. Zhang, X. Wang, L. Cheng, Y. Lou, J. Chen, Micro-meso-  
535 macroporous FeCo-N-C derived from hierarchical bimetallic FeCo-ZIFs as cathode catalysts  
536 for enhanced Li-O<sub>2</sub> batteries performance, *J. Energy Chem.* 35 (2019) 212-219.
- 537 [29] J. Shui, Y. Lin, J. W. Connell, J. Xu, X. Fan, L. Dai, Nitrogen-Doped Holey Graphene for High-  
538 Performance Rechargeable Li-O<sub>2</sub> Batteries, *ACS Energy Lett.* 1 (2016) 260-265.
- 539 [30] X. Huang, H. Yu, H. Tan, J. Zhu, W. Zhang, C. Wang, J. Zhang, Y. Wang, Y. Lv, Z. Zeng, D.  
540 Liu, J. Ding, Q. Zhang, M. Srinivasan, P. M. Ajayan, H. H. Hng, Q. Yan, Carbon Nanotube-  
541 Encapsulated Noble Metal Nanoparticle Hybrid as a Cathode Material for Li-Oxygen Batteries,  
542 *Adv. Funct. Mater.* 24 (2014) 6516-6523.
- 543 [31] H.D. Lim, H. Song, J. Kim, H. Gwon, Y. Bae, K.-Y. Park, J. Hong, H. Kim, T. Kim, Y.H. Kim,  
544 X. Lepró, R.O. Robles, R.H. Baughman, K. Kang, Superior Rechargeability and Efficiency of  
545 Lithium-Oxygen Batteries: Hierarchical Air Electrode Architecture Combined with a Soluble  
546 Catalyst, *Angew. Chem. Int. Ed.* 53 (2014) 3926-3931.
- 547 [32] Y. Chen, S.A. Freunberger, Z. Peng, O. Fontaine; P.G. Bruce, Charging a Li-O<sub>2</sub> battery using a  
548 redox mediator, *Nat. Chem.* 5 (2013) 489-494.
- 549 [33] B.J. Bernger, A. Schürmann, K. Peppeler, A. Garsuch, J. Janek, TEMPO: A Mobile Catalyst for

550 Rechargeable Li-O<sub>2</sub> Batteries, *J. Am. Chem. Soc.* 136 (2014) 15054-15064.

551 [34] Y. Du, Y. Li, B. Xu, T. Liu, X. Liu, F. Ma, X. Gu, C. Lai, Electrolyte Salts and Additives  
552 Regulation Enables High Performance Aqueous Zinc Ion Batteries: A Mini Review, *Small*  
553 (2021) 2104640.

554 [35] S. Guo, L. Qin, T. Zhang, M. Zhou, J. Zhou, G. Fang, S. Liang, Fundamentals and perspectives  
555 of electrolyte additives for aqueous zinc-ion batteries. *Energy Storage Mater.* 34 (2021) 545-  
556 562.

557 [36] L. Song, L. Zou, X. Wang, N. Luo, J. Xu, J. Yu, Realizing Formation and Decomposition of  
558 Li<sub>2</sub>O<sub>2</sub> on Its Own Surface with a Highly Dispersed Catalyst for High Round-Trip Efficiency  
559 Li-O<sub>2</sub> Batteries, *iScience* 14 (2019) 36-46.

560 [37] Z. Luo, F. Li, C. Hu, D. Li, Y. Cao, K. Scott, X. Gong, K. Luo, Impact of a Gold Nanocolloid  
561 Electrolyte on Li<sub>2</sub>O<sub>2</sub> Morphology and Performance of a Lithium-Oxygen Battery, *ACS Appl.*  
562 *Mater. Interfaces.* 13 (2021) 4062-4071.

563 [38] Z. Luo, F. Li, C. Hu, L. Yin, D. Li, C. Ji, X. Zhuge, K. Zhang, K. Luo, Highly dispersed silver  
564 nanoparticles for performance-enhanced lithium oxygen batteries, *J. Mater. Sci. Technol.* 73  
565 (2021) 171-177.

566 [39] M. S. Kim, Z. Zhang, P. E. Rudnicki, Z. Yu, J. Wang, H. Wang, S. T. Oyakhire, Y. Chen, S. C.  
567 Kim, W. Zhang, D. T. Boyle, X. Kong, R. Xu, Z. Huang, W. Huang, S. F. Bent, L. Wang, J.  
568 Qin, Z. Bao, Y. Cui, Suspension electrolyte with modified Li<sup>+</sup> solvation environment for  
569 lithium metal batteries, *Nat. Mater.* 21 (2022) 445-454.

570 [40] W. Li, J. Liu, D. Zhao, Mesoporous materials for energy conversion and storage devices, *Nat.*  
571 *Rev. Mater.* 1 (2016) 16023.

572 [41] W. Yu, H. Wang, J. Hu, W. Yang, L. Qin, R. Liu, B. Li, D. Zhai, F. Kang, Molecular Sieve  
573 Induced Solution Growth of Li<sub>2</sub>O<sub>2</sub> in the Li-O<sub>2</sub> Battery with Largely Enhanced Discharge  
574 Capacity, *ACS Appl. Mater. Interfaces* 10 (2018) 7989-7995.

575 [42] Y. Ding, G.F. Yin, X.M. Liao, Z. Huang, X. Chen, Y. Yao, J. Li, A convenient route to synthesize  
576 SBA-15 rods with tunable pore length for lysozyme adsorption, *Microporous Mesoporous*  
577 *Mater.* 170 (2013) 45-51.

578 [43] Y. Wang, X. Du, Z. Liu, S. Shi, H. Lv, Dendritic fibrous nano-particles (DFNPs): rising stars  
579 of mesoporous materials. *J. Mater. Chem. A* 7 (2019) 5111-5152.

580 [44] R. K. Biswas, P. Khan, S. Mukherjee, A. K. Mukhopadhyay, J. Ghosh, & K. Muraleedharan,  
581 Study of short range structure of amorphous Silica from PDF using Ag radiation in laboratory  
582 XRD system, RAMAN and NEXAFS, *J. Non Cryst. Solids* 488 (2018) 1-9.

583 [45] L. García-Uriostegui, H. Iván Meléndez-Ortiz, G. Toriz, E. Delgado. Post-grafting and

584 characterization of mesoporous silica MCM-41 with a thermoresponsive polymer TEVS/  
585 NIPAAm/  $\beta$ -cyclodextrin, *Materials Letters* 196 (2017) 26-29.

586 [46] C.T. Kresge, M.E. Leonowicz, W.J.J. Roth, J.C. Vartuli, J.S. Beck. Ordered Mesoporous  
587 Molecular Sieves Synthesized by Liquid-Crystal Template Mechanism, *Nature* 359 (1992)  
588 710-712.

589 [47] J. S. Beck, J. C. Vartuli, W. J. Roth, M. E. Leonowicz, C. T. Kresge, K. D. Schmitt, C. T. W.  
590 Chu, D. H. Olson, E. W. Sheppard, S. B. McCullen, J. B. Higgins, and J. L. Schlenker, A new  
591 family of mesoporous molecular sieves prepared with liquid crystal templates, *J. Am. Chem.*  
592 *Soc.* 114 (1992) 10834-10843.

593 [48] S. Perez-Beltran, G. E. Ramírez-Caballero, P. B. Balbuena, First-Principles Calculations of  
594 Lithiation of a Hydroxylated Surface of Amorphous Silicon Dioxide, *J. Phys. Chem. C* 119  
595 (2015) 16424-16431.

596 [49] L. Johnson, C. Li, Z. Liu, Y. Chen, S. A. Freunberger, P. C. Ashok, B. B. Praveen, K. Dholakia,  
597 J.-M. Tarascon, P. G. Bruce, The role of LiO<sub>2</sub> solubility in O<sub>2</sub> reduction in aprotic solvents and  
598 its consequences for Li-O<sub>2</sub> batteries, *Nat. Chem.* 6 (2014) 1091-1099.

599 [50] X. Gao, Y. Chen, L. Johnson, P. G. Bruce, Promoting solution phase discharge in Li-O<sub>2</sub> batteries  
600 containing weakly solvating electrolyte solutions, *Nat. Mater.* 15 (2016) 882-888.

601 [51] Y. Zhou, Z.Y. Lyu, L. Wang, W. Dong, W. Dai, X. Cui, Z. Hao, M. Lai, W. Chen, Co<sub>3</sub>O<sub>4</sub>  
602 functionalized porous carbon nanotube oxygen-cathodes to promote Li<sub>2</sub>O<sub>2</sub> surface growth for  
603 improved cycling stability of Li-O<sub>2</sub> batteries. *J. Mater. Chem. A* 5 (2017) 25501-25508.

604 [52] A. Köllisch-Mirbach, I. Park, M. Hegemann, E. Thome, H. Baltruschat, Electrochemical  
605 Reduction of O<sub>2</sub> in Ca<sup>2+</sup>-Containing DMSO: Role of Roughness and Single Crystal Structure,  
606 *ChemSusChem*, 14 (2021) 2564-2575.

607 [53] X. Zhang, L. Guo, L. Gan, Y. Zhang, J. Wang, L. R. Johnson, P. G. Bruce, Z. Peng, LiO<sub>2</sub>:  
608 Cryosynthesis and Chemical/Electrochemical Reactivities, *J. Phys. Chem. Lett.* 8 (2017) 2334-  
609 2338.